

A mode matching approach for modeling two dimensional porous grating with infinitely rigid or soft inclusions

Benoit Nennig,^{a)} Ygaël Renou, Jean-Philippe Groby, and Yves Aurégan
Laboratoire d'Acoustique de l'Université du Maine, UMR6613 CNRS/Univ. du Maine, Avenue Olivier Messiaen, 72085 Le Mans Cedex 9, France

(Received 2 September 2011; revised 3 February 2012; accepted 19 February 2012)

This work investigates the acoustical properties of a multilayer porous material in which periodic inclusions are embedded. The material is assumed to be backed by a rigid wall. Most of the studies performed in this field used the multipole method and are limited to circular shape inclusions. Here, a mode matching approach, more convenient for a layered system, is adopted. The inclusions can be in the form of rigid scatterers of an arbitrary shape, in the form of an air-filled cavity or in the form of a porous medium with contrasting properties. The computational approach is validated on simple geometries against other numerical schemes and with experimental results obtained in an anechoic room on a rigid grating embedded in a porous material made of 2 mm glass beads. The method is used to study the acoustic absorption behavior of this class of materials in the low frequency range and at a range of angles of incidence. © 2012 Acoustical Society of America. [http://dx.doi.org/10.1121/1.3693655]

PACS number(s): 43.55.Ev, 43.20.Fn, 43.20.Ks, 43.20.Gp [KVVH]

Pages: 3841–3852

I. INTRODUCTION

Porous materials are widely used in noise control applications because of their good sound absorbing properties in the middle and high frequency range. However, their low frequency sound absorbing properties are limited when the layer thickness becomes considerably less than the wavelength. A common practical solution here has been to make use of multilayer materials¹ to reduce the thickness of the overall porous structure and to improve its acoustic absorption properties. Another alternative solution is to embed inclusions into the porous layer to provide additional energy scattering and dissipation mechanisms.² The purpose of this paper is to investigate more systematically the sound absorption properties of embedded periodic inclusions in a porous layer with an numerical technique. The proposed approach is based on the mode matching method.

The idea of using inclusions in porous media is not entirely new. Perforations (i.e., air inclusion) have been exploited in the past to improve the sound absorption of porous material with high flow resistivity. Two distinct approaches were used in normal incidence for the so called double porosity material: (1) using finite element method (FEM)^{3–5} possibly combined with a topological optimization algorithm;⁶ (2) using homogenization.^{7,8} This model has recently been adapted by Gourdon *et al.*⁹ to account for porous material inclusions instead of air cavities. Some noticeable enhancements of the vibro-acoustical properties of the porous materials have been obtained for transparency applications.

All previous models are limited to normal incidence but the oblique case may be investigated thanks to the Floquet-Bloch formalism assuming periodic heterogeneities. This idea was investigated by Groby *et al.* in Ref. 2 for the prediction of the acoustic absorption properties of an heterogeneous porous layer with hard backing. The latter work is mainly concerned with circular rigid inclusions (see Ref. 10 and 11).

In these and other works only few attempts have been made to investigate the effects of an rigid inclusion shape on the acoustic absorption coefficient. In this regard, Allard *et al.*¹² have proposed a layered mode matching approach to study arbitrary corrugated porous materials. Nevertheless, this method have been developed to predict the effect of porous inclusions. When dealing with rigid inclusions, the model must be improved in order to take into account more accurately the presence of geometrical singularity such as corners.¹⁴

One possibility is to make use of orthogonal polynomial basis and in particular their relation to singular weighted function¹³ (Chap. 22) and then to combine them with the modal expansion that will take into account the velocity singularity at corners. A more general method¹⁵ exists which is directly relevant to the solution of the above problem. The idea behind this method has been exploited by Evans and Fernyhough¹⁶ for waves along a periodic coastline or by Homentcovschi *et al.*¹⁷ for waveguide discontinuity problems. This approach is extensively used throughout this paper.

The focus of this paper is on the analysis of heterogeneous inclusions of arbitrary shape embedded in homogeneous porous layers. These heterogeneities can either be air cavities, contrasting porous fillings or rigid scatterers. The proposed layered mode matching scheme is somewhat similar to that presented in Ref. 12 but is able to model properly rigid inclusions.

The method can be used to tackle a generalized case of multilayer structures where all layers can be treated as

^{a)} Author to whom correspondence should be addressed. Present address: Laboratoire d'Ingénierie des Systèmes Mécaniques et des Matériaux (LISMM), SUPMECA, 3 rue Fernand Hainaut, 93407 Saint-Ouen, France. Electronic mail: benoit.nennig@supmeca.fr

heterogeneous. This approach seems to be a good compromise between the computational time and configuration diversity when benchmarked against the finite element method. Compared to homogenization, there is no constraint for the ratio of the size of the heterogeneities to the acoustic wavelength which the method is able to consider.

The present paper is organized as follows. The proposed enhanced mode matching method is presented in Sec. II. In Sec. III, the validity and the accuracy of this method is studied with comparison against other computation methods and measurements. The experimental data are obtained for a periodic gratings with square rigid inclusion embedded in a porous material composed of loose glass beads. In the last section, various numerical examples of increasing complexity are presented.

II. FORMULATION OF THE METHOD

A. Problem statement

We consider that an acoustic plane wave is incident at the oblique angle of incidence on a system of porous layers. We assume that system of layers is periodic in the direction x_1 and that the spatial period is d (see Fig. 1). We assume that the total number of layers stacked up in the direction x_2 is $N_{\mathcal{L}}$. We allow for some heterogeneities to be present within this stack so that a horizontal layer can be split into several sub-layers to represent these heterogeneities as illustrated in Fig. 1. Specifically, we assume that when the propagating wave encounters a pair of vertical rigid walls in the layer \mathcal{L}^i , then the layer must be split, into $N_{\mathcal{C}}^i$ cells such $\mathcal{L}^i = \bigcup_{j=1}^{N_{\mathcal{C}}^i} \mathcal{C}^{i,j}$. We also allow for different materials $\Omega^{i,j}$ to be included in each cell. A new cell $\mathcal{C}^{i,j}$ have to be added each time independent wave propagation can occurred in a layer \mathcal{L}^i , i.e., when vertical rigid walls are present. The interface $\Gamma^i (i = 0, \dots, N_{\mathcal{L}})$ between two layers can be inhomogeneous. It can also be partly rigid interface. The surrounding domain Ω^0 is filled with air with the sound speed c^0 and density ρ^0 .

The skeleton of the porous material is considered to be infinitely rigid, therefore the Champoux-Allard-Johnson

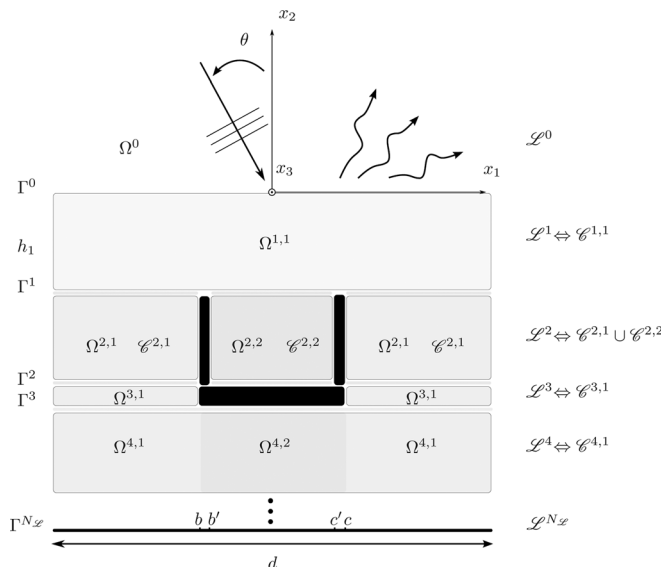


FIG. 1. Geometry of the periodic cell.

equivalent fluid model¹ can be used to predict the equivalent bulk modulus $K^{i,j}$ and the dynamic density $\rho^{i,j}$ (see the Appendix for details). In this case, the wave speed in the domain $\Omega^{i,j}$ is given by the ratio $c^{i,j} = \sqrt{K^{i,j}/\rho^{i,j}}$. The expression for the acoustic pressure, p , in the equivalent fluid (resp. in the fluid) in each of the system domains, $\Omega^{i,j}$, satisfies the harmonic wave equation (the time dependence $e^{-i\omega t}$ is assumed here)

$$\Delta p(x) + (k^{i,j})^2 p(x) = 0, \quad (1)$$

where the wavenumber is defined by $k^{i,j} = \omega/c^{i,j}$.

Since the geometry is periodic along x_1 and the excitation is by a plane wave, $p^{\text{inc}} = A_0 e^{ik_1 x}$, each physical variable within this system X should satisfy the Floquet-Bloch relation

$$X(x_1 + d, x_2) = X(x_1, x_2) e^{ik_1 d}, \quad (2)$$

where the incident wavenumber is $\mathbf{k} = (k_1, k_2) = k^0 \cdot (\sin \theta, -\cos \theta)$. For the sake of conciseness, $\vartheta = e^{ik_1 d}$ and ϑ^* will be used.

We are looking to predict the sound pressure field anywhere in the system of porous layers shown in Fig. 1. As the problem is separable in each layer \mathcal{L}^i , the pressure can be written in the form

$$p^i(x) = \chi(x_1) \mathcal{Y}(x_2), \quad \forall x \in \mathcal{L}^i. \quad (3)$$

In the surrounding fluid domain Ω^0 , the radiation condition, Floquet condition (2) and the separation of variables (3) lead to¹⁸

$$p^0(x) = \sum_{n \in \mathbb{Z}} A_n \frac{1}{\sqrt{d}} e^{i\alpha_n x_1} e^{i\beta_n x_2} + p^{\text{inc}}, \quad \forall x \in \Omega^0, \quad (4)$$

where $\alpha_n^0 = k_1 + n \frac{2\pi}{d}$ and $\beta_n^0 = \sqrt{(k^0)^2 - (\alpha_n^0)^2}$. The axial wavenumber β_n^0 can be real (i.e., a propagating wave) or imaginary (i.e., an evanescent wave). When an incident wave impinges on a periodic, non-planar surface, the scattered waves are spread in discrete directions which depends whether a mode is propagating or not. If $\beta_n^0 = 0$, the mode is said to be resonant,¹⁸ and scattered waves can propagate along the material interface.

In the case of a heterogeneous absorbing material, the above formalism needs a more detailed explanation. The sound pressure in a porous layer \mathcal{L}^i which consists of several sub-domains is effectively a combination of the sound pressures in all the cells $\mathcal{C}^{i,j}$ of this layer, i.e.,

$$p^i(x) = \bigcup_{j=1}^{N_{\mathcal{C}}^i} p^{i,j}(x), \quad \forall x \in \mathcal{L}^i, \quad (5)$$

where, the sound pressure field in the cell $\mathcal{C}^{i,j}$ is sought using the modal expansion

$$p^{i,j}(x) = \sum_{n \in \mathbb{N}} \left(A_n^{i,j} \chi_n^{i,j}(x_1) e^{i\beta_n^{i,j} x_2} + B_n^{i,j} \chi_n^{i,j}(x_1) e^{-i\beta_n^{i,j} x_2} \right), \quad \forall x \in \mathcal{C}^{i,j}. \quad (6)$$

Here, $A_n^{i,j}$ and $B_n^{i,j}$ are the $x_2 > 0$ and $x_2 < 0$ traveling wave amplitudes, respectively. $\chi_n^{i,j}$ and $\beta_n^{i,j}$ are the eigenfunctions

and the eigenvalues, respectively. These latter satisfy the Helmholtz equation (1) and the Floquet-Bloch relation (2). Details on their calculation are given in the following section.

The velocity along x_2 axis, $v^{i,j} = \frac{1}{i\omega\rho^{i,j}} \partial_{x_2} p^{i,j}$, is given by the following series

$$v^{i,j}(x) = \sum_{n \in \mathbb{N}} \left(A_n^{i,j} \chi_{n,v}^{i,j}(x_1) e^{i\beta_n^{i,j} x_2} - B_n^{i,j} \chi_{n,v}^{i,j}(x_1) e^{-i\beta_n^{i,j} x_2} \right), \quad \forall x \in \mathcal{C}^{i,j}, \quad (7)$$

where $\chi_{n,v}^{i,j}(x_1) = \frac{1}{\omega\rho^{i,j}} \beta^{i,j} \chi_n^{i,j}(x_1)$. Similarly to the sound pressure, the velocity in the layer \mathcal{L}^i is defined by

$$v^i(x) = \bigcup_{j=1}^{N_i} v^{i,j}(x), \quad \forall x \in \mathcal{L}^i. \quad (8)$$

In the above summations, the origin of the x_2 is fixed at the upper material surface Γ^0 .

B. Sound field in a periodic cell

Here we focus on the periodic cell which is illustrated in Fig. 1. We will determine the eigenmodes and use them to predict the sound pressure and velocity with the normal mode decomposition method proposed in the previous section.

1. Simple layer

Let us consider the first and unique homogeneous cell within the layer \mathcal{L}^1 (see Fig. 1). As previously mentioned, all the physical variables must satisfy the 1-D Helmholtz equation (1). This yields

$$\chi(x_1) = Ae^{i\alpha x_1} + Be^{-i\alpha x_1}. \quad (9)$$

Applying the Floquet-Bloch relation (2) on the pressure and the velocity¹⁹ (see Sec. III B 2), we get

$$\chi(x_1 + d) = \chi(x_1)\vartheta, \quad (10a)$$

$$\partial_{x_1} \chi(x_1 + d) = \partial_{x_1} \chi(x_1)\vartheta, \quad (10b)$$

leading to the eigenvalue problem

$$\begin{pmatrix} \vartheta - e^{i\alpha d} & \vartheta - e^{-i\alpha d} \\ \vartheta - e^{i\alpha d} & -\vartheta + e^{-i\alpha d} \end{pmatrix} \begin{pmatrix} A \\ B \end{pmatrix} = \begin{pmatrix} 0 \\ 0 \end{pmatrix}. \quad (11)$$

The dispersion equation is

$$(1 - \vartheta^2) + 2\vartheta \cos \alpha d = 0, \quad (12)$$

and its solutions are $\alpha_n = \pm(n\frac{2\pi}{d} + k_1)$ with $n \in \mathbb{Z}$. The wavenumber along x_2 is given by $\beta_n = \sqrt{(k^{i,j})^2 - \alpha_n^2}$. Therefore, only the positive α_n is needed to determine the corresponding wavenumbers β_n . The eigenfunctions are given by

$$\chi_n(x_1) = \frac{1}{\sqrt{d}} e^{i(\pm k_1 + n\frac{2\pi}{d})x_1}. \quad (13)$$

In this special case χ_n represent propagating waves as in Ω^1 along x_1 .

2. Sound propagation in a layer with a rigid inclusion

Consider now the cell $\mathcal{C}^{2,1}$ which belongs to the layer \mathcal{L}^2 (see Fig. 1). This domain is split into two parts because of the presence of a rigid inclusion at $x_1 \in [b, c]$. Two boundary conditions which need to be added to Eq. (10) are

$$\partial_{x_1} \chi(b) = 0, \quad (14a)$$

$$\partial_{x_1} \chi(c) = 0. \quad (14b)$$

It is necessary for the eigenmodes to satisfy the 1-D Helmholtz equation (1), so that

$$\chi(x_1) = \begin{cases} Ae^{i\alpha x_1} + Be^{-i\alpha x_1} & \text{if } x_1 \in [0, b], \\ A'e^{i\alpha x_1} + B'e^{-i\alpha x_1} & \text{if } x_1 \in [c, d]. \end{cases} \quad (15)$$

Applying the boundary conditions from Eq. (14) and Eq. (10) leads to $B = Ae^{2i\alpha b}$, $B' = A'e^{2i\alpha c}$ and

$$\begin{pmatrix} (1 + e^{2i\alpha b})\vartheta & -(\vartheta + e^{2i\alpha c})\vartheta^* \\ (1 - e^{2i\alpha b})\vartheta & -(\vartheta - e^{2i\alpha c})\vartheta^* \end{pmatrix} \begin{pmatrix} A \\ A' \end{pmatrix} = \begin{pmatrix} 0 \\ 0 \end{pmatrix}. \quad (16)$$

The determinant of this system yields $\sin \alpha(d-a) = 0$ with $a = c - b$. The solutions are $\alpha_n = \frac{n\pi}{(d-a)}$ as in the normal incidence case. However, the eigenfunctions are modified by the Floquet-Bloch relation and we get $A' = (-1)^n \vartheta e^{-i\alpha_1 a} A$. Now let us focus on the cell $\mathcal{C}^{2,2}$ embedded in the layer \mathcal{L}^2 . The solution here is somewhat simpler because the eigenproblem is independent of the periodic conditions. In this case, the eigenmodes are similar to those determined for the case of a standard rigid cavity,²⁰ i.e., $\chi_n(x_1) = \cos \alpha_n x_1$ for $x_1 \in [b', c']$ with $\alpha_n = n\pi/d'$ letting $d' = c' - b'$.

3. Sound propagation in a layer with a fluid/porous inclusion

Consider now the cell $\mathcal{C}^{4,1}$ which belongs to the layer \mathcal{L}^4 (see Fig. 1). This cell is split into two parts because of the presence of another material in $\Omega^{4,2}$, which can be a fluid or a porous material with contrasting properties. The boundary conditions are given by the Floquet-Bloch relation (10) and the continuity conditions at a fluid/fluid interface are

$$p^{4,1}(b) = p^{4,2}(b), \quad p^{4,1}(c) = p^{4,2}(c), \quad (17a)$$

$$u^{4,1}(b) = u^{4,2}(b), \quad u^{4,1}(c) = u^{4,2}(c). \quad (17b)$$

Here $u^{i,j} = \frac{1}{i\omega\rho^{i,j}} \partial_{x_1} p^{i,j}$ is the acoustic velocity along the x_1 axis. The corresponding eigenmodes are determined from

$$\chi(x_1) = \begin{cases} A_1 e^{i\alpha_1 x_1} + B_1 e^{-i\alpha_1 x_1} & \text{if } x_1 \in [0, b], \\ A_2 e^{i\alpha_2 x_1} + B_2 e^{-i\alpha_2 x_1} & \text{if } x_1 \in [b, c], \\ A'_1 e^{i\alpha_1 x_1} + B'_1 e^{-i\alpha_1 x_1} & \text{if } x_1 \in [c, d]. \end{cases} \quad (18)$$

From (17) $A' = Ae^{i(k_1 - \alpha_1)d}$, and $B' = Be^{i(k_1 + \alpha_1)d}$ it follows that

$$\begin{pmatrix} e^{i\alpha_1 a} & e^{-i\alpha_1 a} & -e^{i\alpha_2 a} & -e^{-i\alpha_2 a} \\ \frac{\alpha_1}{\rho_1} e^{i\alpha_1 a} & -\frac{\alpha_1}{\rho_1} e^{-i\alpha_1 a} & -\frac{\alpha_2}{\rho_2} e^{i\alpha_2 a} & \frac{\alpha_2}{\rho_2} e^{-i\alpha_2 a} \\ e^{i\alpha_1 b} e^{i(k_1 - \alpha_1)d} & e^{-i\alpha_1 b} e^{i(k_1 + \alpha_1)d} & -e^{i\alpha_2 b} & -e^{-i\alpha_2 b} \\ \frac{\alpha_1}{\rho_1} e^{i\alpha_1 b} e^{i(k_1 - \alpha_1)d} & -\frac{\alpha_1}{\rho_1} e^{-i\alpha_1 b} e^{i(k_1 + \alpha_1)d} & -\frac{\alpha_2}{\rho_2} e^{i\alpha_2 b} & \frac{\alpha_2}{\rho_2} e^{-i\alpha_2 b} \end{pmatrix} \begin{pmatrix} A_1 \\ B_1 \\ A_2 \\ B_2 \end{pmatrix} = \begin{pmatrix} 0 \\ 0 \\ 0 \\ 0 \end{pmatrix}. \quad (19)$$

After the substitution $\alpha_1 = \sqrt{(k^{4,1})^2 - (\beta^4)^2}$ and $\alpha_2 = \sqrt{(k^{4,2})^2 - (\beta^4)^2}$, the determinant of this system yields the dispersion equation with respect to β^4 . In this case, the solutions are not known and numerical methods must be used. We use the algorithm proposed in Ref. 21, which requires an analytic dispersion equation but no initial guess thanks to the winding number (WN) technique. This technique is used to find the roots β_n^i at the first frequency, and these roots are then used as an initial guess for the next frequency step using the Newton-Raphson (NR) algorithm, which is faster but less robust. If the NR algorithm fails, the WN technique is then used instead. This strategy takes the advantage of the both algorithms in terms of its robustness and computational time. It is worth noting that the derivatives are computed analytically to fully take advantage of the NR quadratic convergence property. Once the eigenvalues are found, the eigenmodes can be obtained with a singular value decomposition or another technique. The eigenfunctions are orthogonal if the cell is symmetric.¹² This property is not used directly in this paper but contributes to the robustness of the proposed method. Further details on the orthogonality problem arising in dissipative media are given in Refs. 22 and 23.

C. Mode matching strategy

At each layer interface $\Gamma^i (i = 0, \dots, N_{\mathcal{L}} - 1)$, the condition of the continuity of the pressure and of the normal velocity apply. On the rigid backing, i.e., at interface $\Gamma^{N_{\mathcal{L}}}$, the normal velocity must vanish. The modal expansions, given in Eqs. (5) and (8) can be truncated to N first terms for all the layers. The correspondence $n \leftrightarrow \beta_n^{i,j}$ is given by organizing the imaginary part of the eigenvalues in ascending order so that the lowest attenuation modes are always included in the series. In this work two mode matching schemes have been used: (1) the classical mode matching scheme¹² was used in the case of soft inclusions such as air or another porous material; (2) the mode re-expansion method^{16,17} was used in the case of rigid inclusions. These two numerical schemes are detailed below.

1. The classical mode matching scheme

Let us define

$$\chi^i(x) = \bigcup_{j=1}^{N_i} \chi_n^{i,j}(x), \forall x \in \mathcal{L}^i, \quad (20)$$

to be the expression for the n -th modal profile along the material interface. Matching conditions between the layers are imposed in a weighted sense, i.e., we proceed by choosing a weighting function and then integrate over the interface Γ^i

$$\int_0^d \chi_m^{i,\dagger} (p^i - p^{i+1}) dx_1 = 0, \quad (21a)$$

$$\int_0^d \chi_{m,v}^{i+1,\dagger} (v^i - v^{i+1}) dx_1 = 0. \quad (21b)$$

Here, the weighting functions χ_m^i and $\chi_{m,v}^{i+1}$ are the complex conjugate (denoted by \dagger) eigenfunction of the layer i and of the layer $i + 1$, respectively.²⁴

Using (5) to (8) leads to the overlap integrals matrices

$$\left(P^{(j)} \right)_{m,n} = \int_0^d (\chi_m^i)^{\dagger} \chi_n^j dx_1, \quad (22)$$

and

$$\left(V^{(j)} \right)_{m,n} = \int_0^d (\chi_{m,v}^{i+1})^{\dagger} \chi_{n,v}^j dx_1, \quad (23)$$

where the subscripts m and n are in the $[0, N]$ range. For generality, these integrals are computed numerically using the Gauss-Legendre quadrature rule, although their analytical forms for some special cases can be found in Ref. 12. We note that $8N$ Gaussian quadrature points are used here.

Using previous equations, the scattering system at the interface Γ_i becomes

$$\mathbf{X}^i \mathbf{E}_X \begin{pmatrix} \mathbf{A}^i \\ \mathbf{B}^{i+1} \end{pmatrix} = \mathbf{Y}^i \mathbf{E}_Y \begin{pmatrix} \mathbf{B}^i \\ \mathbf{A}^{i+1} \end{pmatrix}, \quad (24)$$

where the vectors \mathbf{A}^i , \mathbf{B}^i contain the modal amplitudes and the diagonal matrices \mathbf{E}_X and \mathbf{E}_Y contain the phase factor, i.e.,

$$\mathbf{E}_X = \text{diag} \left(e^{i\beta_1^i h_i} \dots e^{i\beta_N^i h_i}, e^{-i\beta_1^{i+1} h_i} \dots e^{-i\beta_N^{i+1} h_i} \right), \quad (25a)$$

$$\mathbf{E}_Y = \text{diag} \left(e^{-i\beta_1^i h_i} \dots e^{-i\beta_N^i h_i}, e^{i\beta_1^{i+1} h_i} \dots e^{i\beta_N^{i+1} h_i} \right). \quad (25b)$$

The matrices \mathbf{X}^i and \mathbf{Y}^i in the above equations are given by

$$\mathbf{X}^i = \begin{pmatrix} \mathbf{P}^{(i)} & -\mathbf{P}^{(i+1)} \\ \mathbf{V}^{(i)} & \mathbf{V}^{(i+1)} \end{pmatrix}, \quad (26a)$$

$$\mathbf{Y}^i = \begin{pmatrix} -\mathbf{P}^{(i)} & \mathbf{P}^{(i+1)} \\ \mathbf{V}^{(i)} & \mathbf{V}^{(i+1)} \end{pmatrix}, \quad (26b)$$

respectively.

2. The re-expansion matching scheme

When rigid inclusions are present, the re-expansion matching scheme is more robust than the classical one. We follow the approach used by Homentcovschi¹⁷ for the computation of the scattering matrix for the waveguide discontinuity problem. This method is detailed for the case with one inclusion per layer as illustrated on Fig. 2. If more rigid inclusions are present, then the method can be easily extended.

The first step is to introduce an auxiliary normal velocity field at the interface Γ^i for $x_1 \in [b, c]$ under the series expansion

$$\tilde{v}(x_1) = w(x_1) \sum_{k=0}^K V_k C_k^v(x_1), \quad (27)$$

with the weight function

$$w(x_1) = [(c - x_1)(x_1 - b)]^{\nu-1/2}. \quad (28)$$

The most important thing is the singular behavior of $w(x_1)$ for $x_1 = b$ and $x_1 = c$, which can be tuned with ν to get the singularity order of the velocity near a corner.¹⁷ We suppose that this singular behavior remains the same for a rigid corner embedded in a porous media or in air, i.e., $\nu = 1/6$. Here V_k are some new auxiliary unknowns, C_k^v are the Gegenbauer polynomials¹³ (Chap. 22) defined for $x_1 \in [b, c]$, which are orthogonal with respect to the weight function $w(x_1)$.

Matching conditions between the layers are imposed in a weighted sense, i.e., we proceed by choosing a weighting function and then integrate over the interface Γ^i . For the pressure continuity condition, the weighting function is $w(x_1)C_k^v(x_1)$. This yields

$$\int_{\gamma_i \cap \gamma_{i+1}} w C_k^v p^i dx_1 = \int_{\gamma_i \cap \gamma_{i+1}} w C_k^v p^{i+1} dx_1. \quad (29)$$

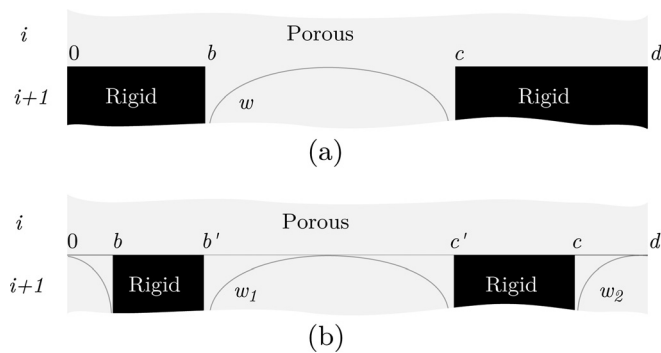


FIG. 2. Details of two rigid-soft interfaces. With one periodic inclusion (a), with two periodic inclusions (b).

The integration support is obviously limited to $\gamma_i \cap \gamma_{i+1}$, where γ_i stands for the support of the modal profile of the layer \mathcal{L}^i . Then, the velocity continuity is applied in two steps: imposing $\tilde{v} = v^i$ and $\tilde{v} = v^{i+1}$ and then by taking the projection of the velocities and their corresponding layer eigenmodes

$$\int_{\gamma_i} \chi_m^i \tilde{v}^i dx_1 = \int_{\gamma_i \cap \gamma_{i+1}} \chi_m^i \tilde{v}^i dx_1, \quad (30a)$$

$$\int_{\gamma_{i+1}} \chi_m^{i+1} \tilde{v}^{i+1} dx_1 = \int_{\gamma_i \cap \gamma_{i+1}} \chi_m^{i+1} \tilde{v}^i dx_1. \quad (30b)$$

In the matrix form it reads as

$$\mathbf{Y}_i (\tilde{\mathbf{B}}^i - \tilde{\mathbf{A}}^i) = \mathbf{D}_i^\dagger \mathbf{V}, \quad (31a)$$

$$\mathbf{Y}_{i+1} (\tilde{\mathbf{B}}^{i+1} - \tilde{\mathbf{A}}^{i+1}) = \mathbf{D}_{i+1}^\dagger \mathbf{V}, \quad (31b)$$

$$\mathbf{D}_i (\tilde{\mathbf{B}}^i + \tilde{\mathbf{A}}^i) = \mathbf{D}_{i+1} (\tilde{\mathbf{B}}^{i+1} + \tilde{\mathbf{A}}^{i+1}), \quad (31c)$$

where \dagger stands for the conjugate transpose matrix, $(\tilde{\mathbf{A}}^i)_n = A_n^i e^{i\beta_n^i h_i}$ and $(\tilde{\mathbf{B}}^i)_n = B_n^i e^{-i\beta_n^i h_i}$ contain the modal amplitudes, \mathbf{V}^i contain the new auxiliary unknowns and

$$(\mathbf{D}_i)_{k,n} = \int_{\gamma_i \cap \gamma_{i+1}} w C_k^v \chi_n^i dx_1, \quad (32a)$$

$$(\mathbf{Y}_i)_{m,n} = \frac{\beta_n^i}{\omega \rho^i} \int_{\gamma_i} \chi_m^i \chi_n^i dx_1. \quad (32b)$$

The above integrals are computed numerically. The choice of the numerical quadrature adopted here is essentially motivated by its relative simplicity and numerical stability. The indices m, n , and k belong to $[0, N]$.

The use of the numerical Gauss-Gegenbauer quadrature rule²⁵ which accounts for the weight function w singularity is very efficient when 8 N Gauss quadrature points are used. In this procedure the recursive definition of the Gegenbauer polynomials (Ref. 13's Table 22.7) can be used to limit the round-off error.

The expressions for the scattering matrices

$$\mathbf{E}_X \begin{pmatrix} \mathbf{A}^i \\ \mathbf{B}^{i+1} \end{pmatrix} = \begin{pmatrix} \mathbf{S}_i^{11} & \mathbf{S}_i^{12} \\ \mathbf{S}_i^{21} & \mathbf{S}_i^{22} \end{pmatrix} \mathbf{E}_Y \begin{pmatrix} \mathbf{B}^i \\ \mathbf{A}^{i+1} \end{pmatrix}, \quad (33)$$

relating the incident and reflected waves at each interface Γ_i have been given in Ref. 17 and are recalled here as

$$\mathbf{S}_i^{11} = (\mathbf{H}_i + \mathbf{D}_i)^{-1} (\mathbf{H}_i - \mathbf{D}_i), \quad (34a)$$

$$\mathbf{S}_i^{22} = (\mathbf{H}_{i+1} + \mathbf{D}_{i+1})^{-1} (\mathbf{H}_{i+1} - \mathbf{D}_{i+1}), \quad (34b)$$

$$\mathbf{S}_i^{21} = 2(\mathbf{D}_{i+1})^{-1} \mathbf{D}_i (\mathbf{H}_i + \mathbf{D}_i)^{-1} \mathbf{H}_i, \quad (34c)$$

$$\mathbf{S}_i^{12} = 2(\mathbf{D}_i)^{-1} \mathbf{D}_{i+1} (\mathbf{H}_{i+1} + \mathbf{D}_{i+1})^{-1} \mathbf{H}_{i+1}, \quad (34d)$$

with

$$\mathbf{H}_i = \mathbf{D}_{i+1} \mathbf{Y}_{i+1}^{-1} \mathbf{D}_{i+1}^\dagger (\mathbf{D}_i^\dagger)^{-1} \mathbf{Y}_i, \quad (35a)$$

$$\mathbf{H}_{i+1} = \mathbf{D}_i \mathbf{Y}_i^{-1} \mathbf{D}_i^\dagger (\mathbf{D}_{i+1}^\dagger)^{-1} \mathbf{Y}_{i+1}. \quad (35b)$$

To get the modal amplitudes we could recombine Eq. (33) and (24) to build a linear system $\mathbf{KA} = \mathbf{F}$, where all the unknowns, gathered in the vector \mathbf{A} , can be deduced from the right hand side of \mathbf{F} arising from the incident wave. However, the inversion of such a system is, unfortunately, subject to round-off errors due to the presence of strongly evanescent waves. Because of these limitations, an alternative iterative procedure, proposed by Cummings²⁶ and used successfully by the authors for silencer modeling,²¹ is adopted here.

The idea is to treat each interface separately by considering all incoming waves as known quantities. At the first iteration, the unknown incoming waves $[\mathbf{B}^i, \mathbf{A}^{i+1}]^t$ are fixed at zero or initialized by a previous frequency step solution. The systems given in Eq. (33) and/or in (24) are then solved for the outgoing waves $[\mathbf{A}^i, \mathbf{B}^{i+1}]^t$. This produces an initial value for the incoming waves on the next interface and so on. This loop over the interface stops when the relative error on modal amplitudes is smaller than 10^{-6} between two consecutive iterations. In practice, around $10 \times N_{\mathcal{G}}$ iterations are required. The factorization of the diagonal matrix \mathbf{E}_X , containing all propagation factors, is one of the main advantages of this iterative process. Indeed, its condition number is very large due to the combination of $x_2 > 0$ and $x_2 < 0$ traveling “evanescent” waves. Thus, inverting \mathbf{E}_X separately minimizes the effects of possible round-off errors. Furthermore, the scattering matrices $X_i (i = 0, \dots, N_{\mathcal{G}})$ are well-conditioned and the condition number can be enhanced by a careful choice of the weighting function in order to maximize their diagonal terms²⁴ as already discussed in Sec. II C 1.

Once the wave amplitudes have been evaluated, the integration of the acoustic intensity leading to the energy balance can be applied. The integration is carried out over the periodic cell using the orthogonality relation of the Floquet modes given in (4). The energy reflection coefficient¹⁸ \mathcal{R} is defined as the ratio of the scattered power in the x_2 direction

$$\mathcal{P}_r = \sum_{n \in \mathbb{Z}} \Re\{\beta_n^0\} |A_n^0|^2 / (\rho^0 \omega), \quad (36)$$

to the incident power

$$\mathcal{P}_i = |A_0|^2 k_2 d / (\rho^0 \omega). \quad (37)$$

In practice, the number of propagating modes in Ω^0 is very small and it is often reduced to the fundamental mode $n = 0$ and the first mode $n = \pm 1$.

Thanks to the conservation of the energy, the absorbed power is given by $\mathcal{P}_{abs} = \mathcal{P}_i - \mathcal{P}_r$. This yields the absorption coefficient

$$\alpha = \frac{\mathcal{P}_{abs}}{\mathcal{P}_i} = 1 - \mathcal{R}. \quad (38)$$

III. VALIDATION AND ACCURACY

In this section the validation and the accuracy of the proposed method is investigated. Firstly, the computational efficiency is studied for the case of a porous layer with rectangular and circular inclusions. Secondly, an experimental validation is performed to check ability of the method to describe accurately the acoustic behavior of a finite size porous layer with inclusions composed of a number of periodic cells.

A. Convergence study on rectangular shaped inclusions

In this example, we consider porous and rigid rectangular inclusions embedded in metal foam (see Table I). Because no solution is available in the literature for this geometry, the reference solutions are computed using a finite element model. These computations are carried out using Lagrange quadratic finite elements in the fluid and porous domains as described in Ref. 12. The non-reflecting boundary conditions are implemented using the Dirichlet to Newman (DtN) approach based on Eq. (4) to avoid problems when the wavelength is high compared with the computational domain size. The reference absorption computations $\hat{\alpha}$ are performed with a mesh of around 280,000 nodes. It can be noted that an equivalent meshing size leads to 8 digits accuracy in the predicted absorption coefficient for homogeneous porous (i.e., without inclusion). In this study the inclusion height was fixed to 15 mm, and two widths, $a = 15$ and $a = 5$ mm, were tested. In both cases, the inclusions were located in the center of the 20 mm \times 20 mm periodic cell. These configurations have been tested at 5000 Hz for 2 incident wave angles, $\theta = 0$ and $\theta = \pi/3$ rad.

With a porous inclusion (RGW2 wool, see Table I), the present method has shown an exponential convergence, and a relative error $\varepsilon = (|\alpha - \hat{\alpha}|) / \hat{\alpha}$ below 1% has been achieved in all tested configurations with 3 modes and the classical matching scheme. With a perfectly rigid inclusion, the classical matching scheme is not numerically stable for large rigid inclusions, and it was not possible to get a relative error below 5% without accounting for at least 30 modes in the summation. It is known that the number of modes could be adapted according to the section ratio^{14,16} to enhance the convergence. However, the re-expansion scheme, described

TABLE I. Material properties used in numerical tests. With the porosity ϕ , flow resistivity σ , the tortuosity α_{inf} , the viscous and thermal characteristic lengths Λ and Λ' .

Material	ϕ	σ [Nm ⁻⁴ s]	α_{inf}	Λ [μ m]	Λ' [μ m]	Reference
Beads	0.4	11,204	1.37	148	444	[28, 29]
Fireflex	0.95	8,900	1.42	180	360	[2]
RGW2	0.94	135,000	2.10	49	166	[4]
Metal foam	0.99	6,916	1.17	100	245	-

in Sec. II C 2, was adopted because it seems faster and more robust. With this scheme, an error smaller than 1% can be achieved with only 3 modes. This accuracy seems sufficient for the applications proposed in this paper.

B. Validation with the multipole method

A comparison with the results presented in Ref. 2 (see Figs. 3 and 4 inside) for rigid circular inclusions has been performed. This kind of geometry can be tackled with the proposed method despite the fact that it is not the more appropriated technique. The multipole² method or the method of fundamental solutions²⁷ constitute better approaches for circular shape inclusion. Here, the circular inclusion of radius a is discretized by 11 layers of rigid rectangular inclusions (see Fig. 4), and $N + 1 = 7$ modes are taken into account in each layer. This level of discretization enables to achieve a good agreement in the frequency range up to 13 kHz with the results of Groby *et al.*² obtained for a similar problem as illustrated on Fig. 5. The presence of such inclusions can enhance the absorption of the Fireflex foam (see Table I), particularly around 2674 Hz where an absorption peak is obtained below the 1/4-wavelength resonance frequency, $f_{\lambda/4}$. This behavior can be explained by the excitation of a complex trapped mode.² At this frequency, the sound pressure maximum is localized near the rigid backing as depicted in Fig. 4. With the proposed modal approach, this rigid scatterer can be easily replaced by glass wool circular inclusions of the same radius (RGW2 wool, see Table I). Obviously, such results can also be obtained with slight modifications to the multipole method.² Above 1500 Hz, this new heterogeneous material exhibited better absorbing properties than any of its constituent materials. It appears that the absorption properties of a heterogeneous porous material are only slightly sensitive to the inclusion shape, e.g., the presence of square inclusions with the same area leads to a similar absorption curve.

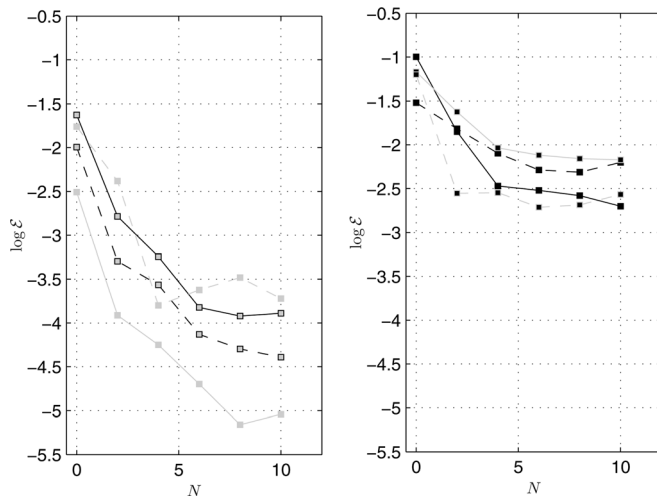


FIG. 3. Convergence of the proposed method for a small ($a/d = 0.25$, $--$) and larger ($a/d = 0.25$, $—$) inclusion size. The black lines stand for the normal incidence and the gray ones for $\theta = \pi/3$. The black \blacksquare -markers stand for the rigid inclusion (see on the right) and the gray \blacksquare -markers for the RGW2 porous inclusion (see on the left).

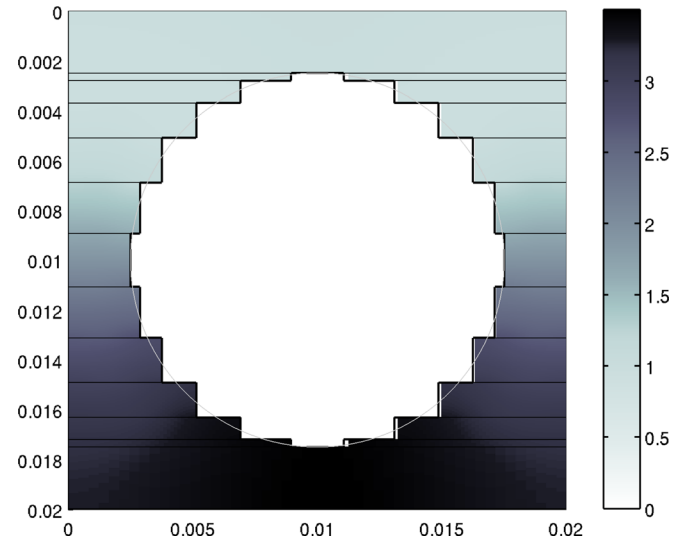


FIG. 4. (Color online) Pressure modulus with the layered rigid circular inclusions at 2674 Hz (first absorption peak of Fig. 5). The horizontal lines stand for the layer interfaces.

C. Experimental validation

An experimental validation has been performed in the anechoic chamber available in LAUM (Laboratoire d'Acoustique de l'Université du Maine, France). The experimental setup is illustrated in Figs. 6 and 7. The tested sample was formed with 25 identical elementary cells of 20 mm width and of 21.5 mm height. These cells were created with a periodic array of 500 mm long, square aluminum bars which were backed by a 4 mm thick aluminum plate attached to a 20 mm thick wooden base. Figure 6 illustrates schematically the arrangement of these bars and the periodic grating which this arrangement recreated. The experimental setup shown in this figure had the following dimensions: $a = 15$ mm, $h = 21.5$ mm, $t_1 = 2.5$ mm, $t_2 = 4$ mm and $d = 20$ mm. The simulated periodic grating (500 mm \times 500 mm) was filled

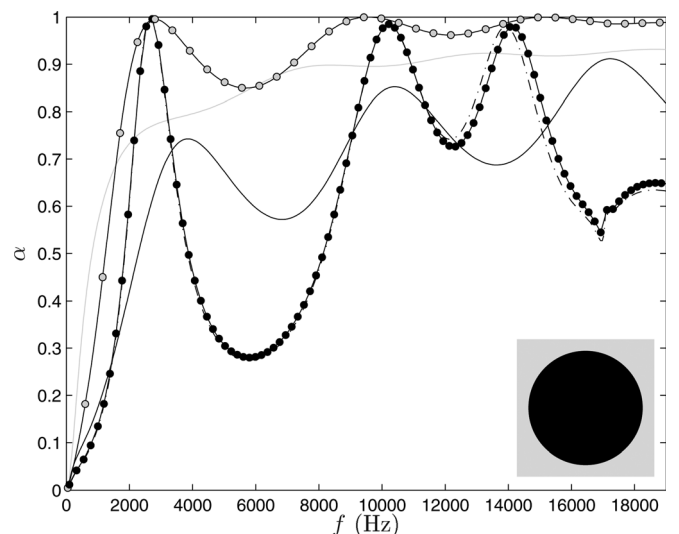


FIG. 5. Comparison and illustration of the proposed method with circular inclusions ($a = 1.5$ cm) on a 2×2 cm cell with 11 Layers. $—$ homogeneous Fireflex material, $- -$ homogeneous RGW2 material, \bullet circular rigid inclusion, \dots circular rigid inclusion from Ref. 10, \bullet circular RGW2 inclusion.

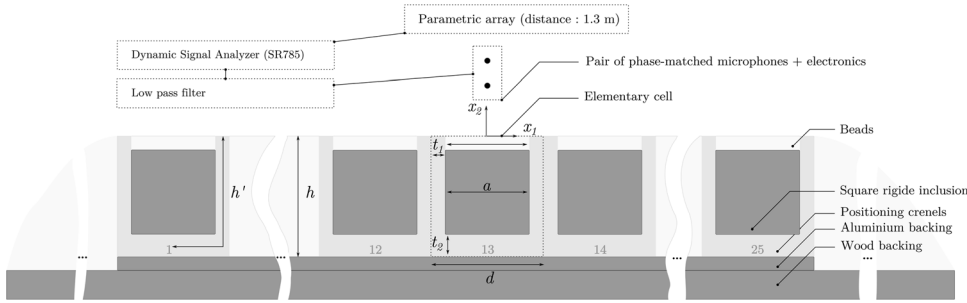


FIG. 6. Schematic description of the experimental setup with the square section.

with 2 mm glass beads (see Fig. 7) to the required thickness. Additional beads were spread around the sample to cover the whole wooden plate (1×1 m). The use of glass beads enabled to create a porous filling around various inclusion shapes. This medium had the basic acoustical and non-acoustical characteristics which were relatively easy to predict. The Johnson-Champoux-Allard properties for these beads are summarized in Table I. The values of these parameters were borrowed from Refs. 28 and 29.

A parametric source array³⁰ (using parametric demodulated ultrasonic waves) was used to create a highly directional plane wave normal to the grating at audible frequencies to control the diffraction from the edges of the periodic grating. The distance between the center of the grating and parametric source array was 1.3 m. A dynamic signal analyzer (SR785) was used to drive the parametric source array with a swept sine. A pair of phase-matched microphones (1/4'' microphones B&K 4938 with B&K 2670 preamplifiers and Nexus 4-channel amplifier) was installed at the center of the grating. The microphone elevations above the center of grating were $h_1 = 8$ mm and $h_2 = 28$ mm, respectively. Below the first cut-off frequency of the Floquet mode (around 17 000 Hz for the 2 cm cell), the energy reflection coefficient was deduced from

$$\mathcal{R}(\omega) = \left| \frac{e^{-2ik^0 h_1} e^{-ik^0(h_2-h_1)} - H(\omega)}{H(\omega) - e^{ik^0(h_2-h_1)}} \right|^2, \quad (39)$$

and the absorption coefficient was computed with Eq. (38).

Here $H(\omega) = \frac{p^0(0, h_2)}{p^0(0, h_1)}$ denotes the frequency transfer function

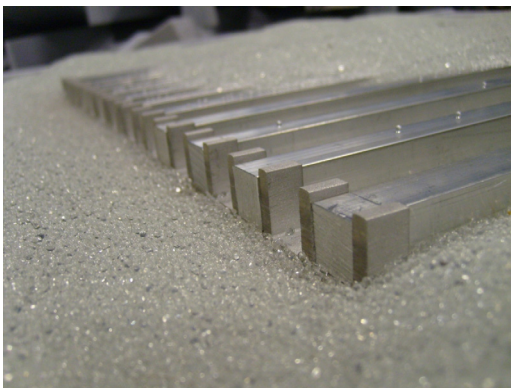


FIG. 7. (Color online) Picture of the experimental setup before total beads and inclusions filling.

between the two microphones located in the middle of the material sample. An analog 20 kHz lowpass Butterworth/Bessel multichannel filter from Krohn-Hite Corporation model # 3945 was used to remove the residual ultrasonic waves emitted by the parametric array.

The comparison of the simulations and experimental data is presented in Fig. 8 for the homogeneous beads and for an array of rigid, square inclusions. In all cases the general behavior of the absorption curves is closely predicted. A good agreement is obtained for the frequency of the first absorption peak and for its amplitude. The discrepancies with the square inclusions are in line with the results obtained in the case of the homogeneous porous layer. The presence of oscillations in the acoustic absorption spectrum is clearly visible in the case of the square inclusions. This can be explained by the edge diffraction effect which relates to the finite size of the simulated periodic grating. This effect is not taken into account by Eq. (39).

In the homogeneous case, the 1/4-wavelength resonance accounts for the absorption peak around $f_{\lambda/4} = 3$ kHz. The use of square rigid inclusions allows for the measurement of a high absorption peak at 2041 Hz, which is below the predicted value of $f_{\lambda/4}$. At this frequency, the absolute part of the sound pressure computed with the proposed method is high and it is localized near the backing wall. In this case, the absorption coefficient at the higher frequencies is relatively

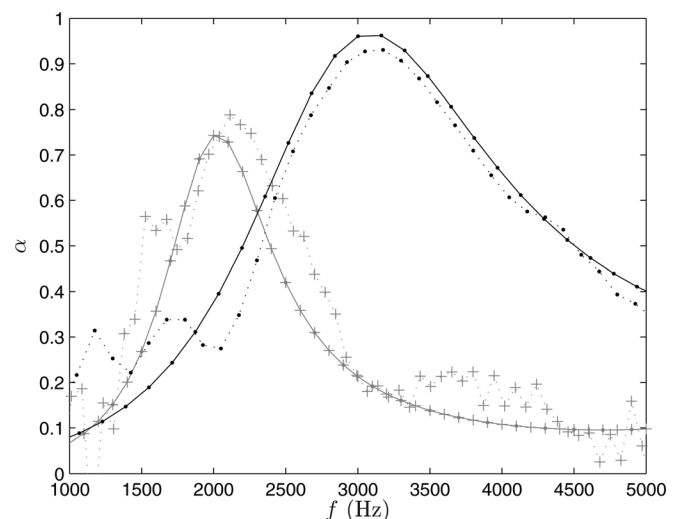


FIG. 8. Comparison between simulations (solid line) and measurements (dotted line) for square shape inclusion (+) and homogeneous beads (·).

poor. An estimation of the absorption peak frequency f_x accurate within a few percent can be obtained with a modified expression for the frequency of the 1/4-wavelength resonance

$$f_x \approx \frac{c}{4h'} \approx 2200 \text{ Hz}, \quad (40)$$

where c is the sound speed in the beads and $h' = (h - t_2/2 + a/2 + t_1/2) = 28.25 \text{ mm}$ corresponds to the apparent length along the square inclusion (see Fig. 6).

IV. NUMERICAL RESULTS ON SQUARE SCATTERER

Numerical calculations of the absorption coefficient have been performed for various inclusion types and shapes. The effect of the angle incidence on the absorption coefficient of this system has also been studied. All computations were performed for metal foam which properties are presented in (see Table I).

A. Inclusion types

In this section, we are interested in square inclusions located in the center of the periodic cell ($20 \text{ mm} \times 20 \text{ mm}$) and excited by a plane wave propagating at the normal angle of incidence. The inclusion height a was varied from 1 mm to 18 mm in a 1 mm step. It was assumed that the inclusions were square, rigid and/or filled with air or with another porous material with contrasting properties (e.g., RGW2). The predicted absorption coefficient for these configurations is shown in Fig. 9.

The results suggest that the air-filled inclusions embedded in this metal foam do not enhanced the acoustic absorbing behavior and that bigger air-filled inclusions result generally in a lower absorption coefficient. This result is predictable, because it is known⁴ that air gaps are efficient only for highly resistive and weakly tortuous porous material such as RGW2. The RGW2-filled inclusions case is more effective. If the inclusions are small, then the behavior is dominated by the metal foam matrix. On the contrary, when the inclusions are large, then the behavior is close to that expected for an homogeneous layer of RGW2 wool. Between these two extreme configurations, the absorption of the heterogeneous material is generally better than the absorption of each of the two homo-

geneous materials considered separately. This stands for the range of the square inclusion height considered in this study ($a \in [10, 18] \text{ mm}$).

The results from this modeling work also show that the absorption coefficient is not too sensitive to the geometry of the embedded porous shape and that the filling ratio seems to be the most significant parameter which accounts for any improvement. These results are in line with those obtained by the homogenization method⁹ or by Nennig *et al.*²⁷ for poroelastic scatterers embedded in air.

For the rigid inclusions case, the results are similar to those presented with the circular inclusions in Sec. III B. If the inclusion's size is sufficiently large, a peak in the absorption spectrum emerges. Hence, in the case of the considered layer configuration, the absorption coefficient may be enhanced between 2000 and 4000 Hz. The absorption coefficient reaches a minimum around 5 kHz. Groby *et al.*² have explained this behavior by the presence of a bandgap of the "underlying" periodic array arising from the perfect reflection on the hard backing. Within this bandgap most of the acoustic energy is reflected backward, i.e., back in the domain Ω^0 , leading to a poor absorption.

B. The effect of the inclusion position

As already shown by Groby *et al.*² that the inclusion position in the periodic cell can be a sensitive parameter. For a given square inclusion ($a = 15 \text{ mm}$), the influence of the inclusion height, t_2 , and the periodic cell width, d , are illustrated in Fig. 10. It can be shown that the absorption frequency increases for larger values of the cell period, d . Moreover, the peak amplitude reaches a maximum for $d \approx 30 \text{ mm}$. Note that sudden variation of the absorption coefficient (the so called Wood's anomalies) can be observed at the first cut-off frequency of the Floquet mode¹⁸ when d is sufficiently large.

The influence of the inclusions height, t_2 , is essentially related to the absorption peak frequency and has nearly no influence on the peak amplitude. When the height t_2 increases, the absorption peak frequency decreases. Once again, this can be explained² by the presence of the "underlying" periodic array formed by the inclusions images with respect to the hard backing. When t_2 increases, the

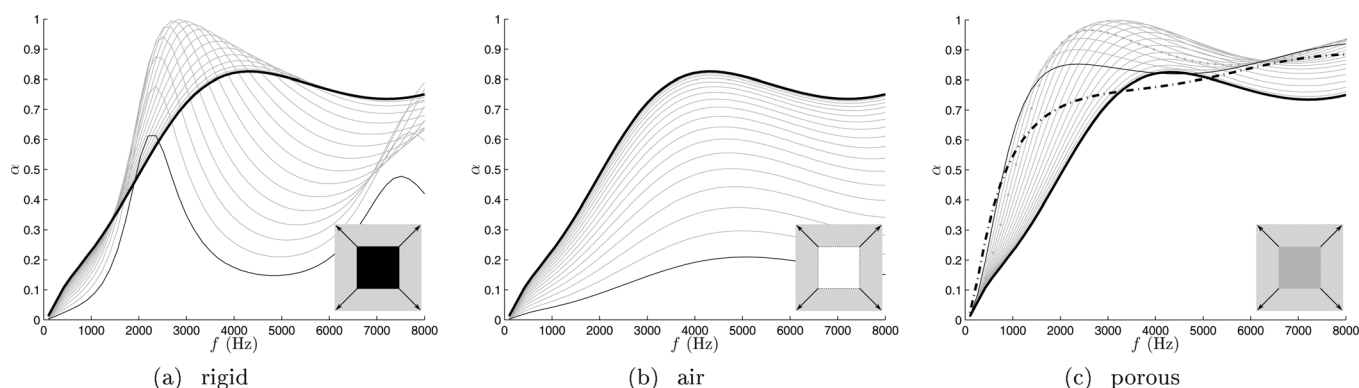


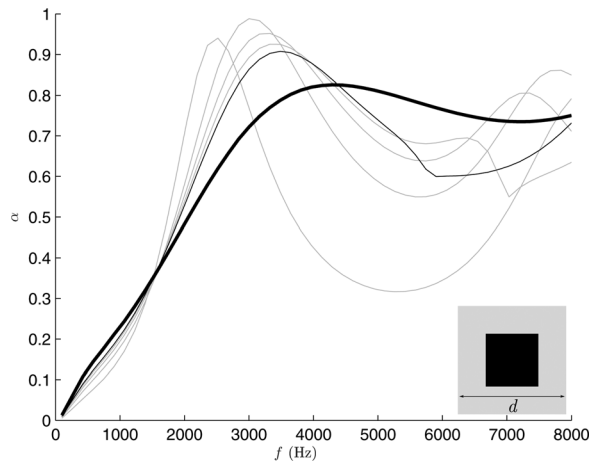
FIG. 9. Effect of the size a of a square inclusion on the absorption coefficient. The inclusion size ranges from 1 to 18 mm in 1 mm step. (—) stands for the upper bound (18 mm) of the variation interval. The reference homogeneous metal foam absorption is denoted by (—) and the RGW2 wool by (- - -). (a) Rigid inclusion, (b) Air inclusion, and (c) RGW2 porous inclusion.

period of the image sonic crystal increases, pushing peaks towards the low frequencies.

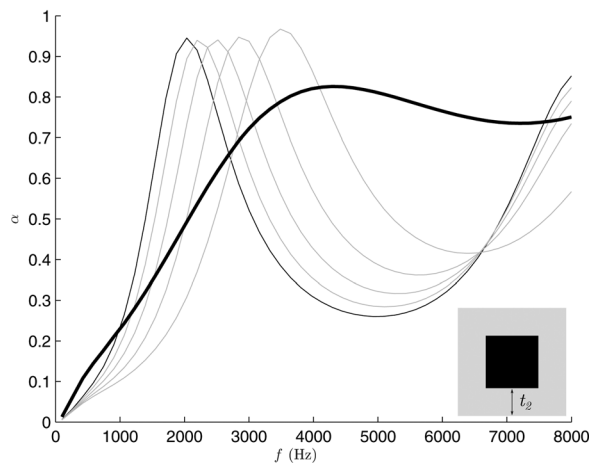
C. Effect of the angle of incidence

The Floquet-Bloch formalism presented in this work enables to study the effect of the angle of incidence θ . The low frequency absorption coefficient of a homogeneous porous layer increases with θ . However, the behavior in the medium and high frequencies depends strongly on the material properties. For example, in the case of metal foam the absorption coefficient drastically decreases with θ above 2000 Hz in comparison with the normal incidence case (see Fig. 11). When the variation of the angle of incidence is small, then the absorption behavior is similar to that predicted for the normal incidence case. In contrast, when the angle of incidence is large (say $\theta > \pi/3$), the absorption can change considerably.

With a rigid square inclusion, this general behavior remains unchanged but the effect of the high value of θ



(a) d from 20 by 10 to 60 mm



(b) t_2 from 0.5 by 1 to 4.5 mm

FIG. 10. (a) Influence of the elementary cell period d and (b) of the inclusions height t_2 on the absorption coefficient with rigid square inclusions (with $a = 15$ mm) grating. The homogeneous metal foam absorption is denoted by (—) in normal incidence. In all cases, (—) stands for the upper bound of the variation interval.

seems to be less significant and the absorption peak frequency typically increases with θ .

V. THE INFLUENCE OF THE INCLUSION SHAPE

Squares or circles are not the optimal inclusions shapes because a large part of the porous matter is removed from the layer. As a result, its broadband absorption capabilities are partially lost. A better approach is to use “open” or “partially open” inclusions, such \sqcup (as illustrated on Fig. 12), to increase the apparent tortuosity of the material and to add more trapped modes. A number of different configurations were studied in this work by changing the \sqcup -section orientation, e.g., \sqcup , \sqcap , or \sqsubset . The acoustic absorption coefficient for a heterogeneous porous layer with these types of inclusions was predicted with the proposed numerical method.

It was found that the absorption coefficient of a porous layer with rigid inclusions is more sensitive to the inclusion shape than that in the case of the layer impregnated with fluid-filled or porous inclusions. For example, the presence of a \sqcap -section in a porous layer yields the lowest absorption peak frequency, i.e. nearly two times smaller than the $f_{\lambda/4}$ frequency predicted for the uniform porous layer. At this frequency the sound pressure modulus near the wall of a rigid \sqcap -shape inclusion is relatively high and strongly localized. However, the absorption coefficient spectra oscillates significantly as a function of frequency.

With the upside-down configuration, i.e., \sqcup -shape, the absorbing coefficient can be greatly enhanced (by more than 20%) across the entire frequency range. This is associated with the presence of two absorption peaks caused by the existence of two trapped modes in the porous layer. One of these modes relates to a localized pressure field between the inclusions and the backing wall. In the case of the second peak, the pressure modulus is localized near the wall inside

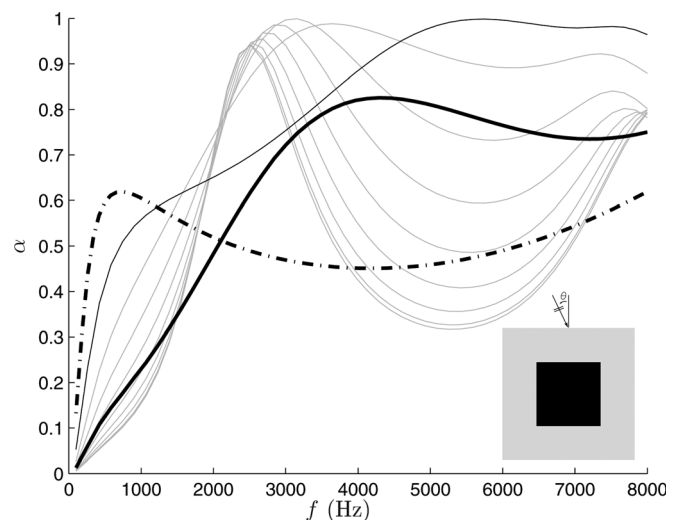


FIG. 11. Effect of the angle of incidence (θ from 0 by 10 to 80°) on the absorption coefficient of a porous layer with rigid square inclusions (with $a = 15$ mm). The homogeneous metal foam material is denoted by (—) in normal incidence and by (---) for $\theta = 80^\circ$. The upper bound of the variation interval (80°) is denoted by (—).

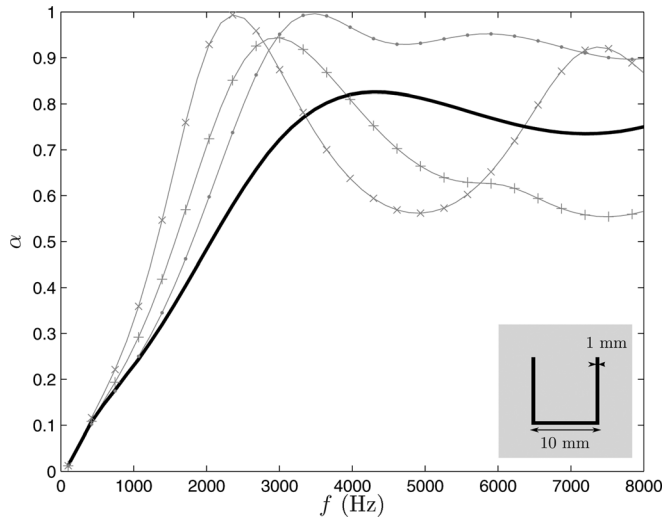


FIG. 12. Effect on the absorption coefficient of the orientation of a rigid \sqcup inclusion embedded in the metal foam ($a=10$ mm, thickness 1 mm). The (\cdot) stand for the \sqcup , the (\times) for the \square and the $(+)$ for the \square orientation. The homogeneous metal foam absorption is denoted by (—) .

the \sqcup inclusion. The \square orientation exhibits a behavior between the two previous cases.

VI. CONCLUSIONS

In this article, a new mode matching scheme is proposed in order to study the acoustical behavior of a multilayer porous material in which periodic inclusions are embedded. The method is validated numerically and experimentally with rigid inclusions embedded in 2 mm beads. It has been shown that taking into account the inclusions geometry is necessary when the inclusions are rigid. The proposed method can tackle a large variety of shapes and inclusion types faster than a conventional FEM model.

This work is an attempt to investigate the influence of the shape of rigid scatterers embedded in a porous material. It has been shown that open shape inclusions (e.g. \sqcup -shape) are able to provide a better effect than inclusions of closed shapes, because less porous material is removed from the layer. These heterogeneous structures can exhibit better acoustic absorption behavior than homogeneous porous layers of identical thickness and provide an alternative to multi-layering.

Future work can focus on exploring new inclusion shapes or more simple shape combinations. In particular, rigid inclusions combined with metal foam is an interesting way to achieve a compact, efficient acoustic treatment for a harsh environment or when good structural behavior is required.

ACKNOWLEDGMENTS

This work was in part financially supported by the FUI project REBECCA. The authors would like to thank their industrial partners Snecma and Snecma Propulsion Solide from Safran group. The authors would like to thank Professor K.V. Horoshenkov for his original idea about the beads

for manufacturing the surrounding porous material and for his comments on this manuscript.

APPENDIX: RIGID FRAME MODEL

Porous materials with a rigid skeleton (and quite regular pore shape), such as the porous material involved in this study, are well described by the Johnson-Champoux-Allard¹ (Chap. 5) equivalent fluid model. This equivalent fluid has the equivalent density ($e^{-i\omega t}$).

$$\rho = \frac{\alpha_\infty \rho^0}{\phi} \left[1 + i \frac{\sigma \phi}{\omega \rho^0 \alpha_\infty} G_J(\omega) \right], \quad (\text{A1})$$

and the bulk modulus,

$$K = \frac{\gamma P^0 / \phi}{\gamma - (\gamma - 1) \left[1 + i \frac{8\eta}{\Lambda'^2 \text{Pr} \omega \rho^0} \left(1 - i \rho^0 \frac{\omega \text{Pr} \Lambda'^2}{16\eta} \right)^{1/2} \right]^{-1}}. \quad (\text{A2})$$

Note that the domain indices i, j are omitted for clarity. Here, $G_J(\omega) = \sqrt{1 - \frac{4i\alpha_\infty^2 \eta \rho^0 \omega}{\sigma^2 \Lambda'^2 \phi^2}}$, ϕ is the porosity, σ is the flow resistivity, Λ is the viscous length, Λ' is the thermal length, α_∞ is the tortuosity. Moreover, γ is the air specific heat ratio and P^0 is the atmospheric pressure, Pr is the Prandtl number and η is the dynamic viscosity. It is important to note, the viscosity is taken into account in the porous material pore but is neglected in the surrounding fluid.

¹J.-F. Allard, *Propagation of Sound in Porous Media: Modeling Sound Absorbing Materials* (Chapman and Hall, New York, 1993), 280 pp.

²J.-P. Groby, A. Duclos, O. Dazel, L. Boeckx, and W. Lauriks, "Enhancing absorption coefficient of a backed rigid frame porous layer by embedding circular periodic inclusions," *J. Acoust. Soc. Am.* **130**, 3071–3780 (2011).

³N. Atalla, R. Panneton, F. C. Sgard, and X. Olny, "Acoustic absorption of macro-perforated porous materials," *J. Sound Vib.* **243**, 659–678 (2001).

⁴F. C. Sgard, X. Olny, N. Atalla, and F. Castel, "On the use of perforations to improve the sound absorption of porous materials," *Appl. Acoust.* **66**, 625–651 (2005).

⁵F. C. Sgard, F. Castel, and N. Atalla, "Use of a hybrid adaptive finite element/modal approach to assess the sound absorption of porous materials with meso-heterogeneities," *Appl. Acoust.* **72**, 157–168 (2011).

⁶J. S. Lee, Y. Y. Kim, J. S. Kim, and Y. J. Kang, "Two-dimensional poroelastic acoustical foam shape design for absorption coefficient maximization by topology optimization method," *J. Acoust. Soc. Am.* **123**, 2094–2106 (2008).

⁷X. Olny and C. Boutin, "Acoustic wave propagation in double porosity media," *J. Acoust. Soc. Am.* **114**, 73–89 (2005).

⁸F.-X. Bécot, L. Jaouen, and E. Gourdon, "Application of the dual porosity theory to irregularly shaped porous materials," *Acta Acust.* **94**, 715–724 (2008).

⁹E. Gourdon and M. Seppi, "On the use of porous inclusions to improve the acoustical response of porous materials: Analytical model and experimental verification," *Appl. Acoust.* **71**, 283–298 (2010).

¹⁰J.-P. Groby, A. Wirgin, L. De Ryck, and W. Lauriks, "Acoustic response of a rigid frame porous medium slab with a periodic set of inclusions," *J. Acoust. Soc. Am.* **126**, 685–693 (2009).

¹¹J.-P. Groby, A. Duclos, O. Dazel, L. Boeckx, and W. Lauriks, "Absorption of a rigid frame porous layer with periodic circular inclusions backed by a periodic grating," *J. Acoust. Soc. Am.* **129**, 3035–3046 (2011).

¹²J.-F. Allard, O. Dazel, G. Gautier, J.-P. Groby, and W. Lauriks, "Prediction of sound reflection by corrugated porous surfaces," *J. Acoust. Soc. Am.* **129**, 1696–1706 (2011).

¹³A. Abramowitz and I. Stegun, *Handbook of Mathematical Functions* (Dover, New York, 1965), 1043 pp.

- ¹⁴J. Kergomard and A. Garcia, "Simple discontinuities in acoustic waveguides at low frequencies: Critical analysis and formulae," *J. Sound Vib.* **114**, 465–479 (1987).
- ¹⁵D. Gottlieb, C.-W. Shu, A. Solomonoff, and H. Vanderen, "On the Gibbs phenomenon I: Recovering exponential accuracy from the Fourier partial sum of a nonperiodic analytic function," *J. Comput. Appl. Math.* **43**, 81–98 (1992).
- ¹⁶V. Evans and M. Fernyhough, "Edge waves along periodic coastlines. Part 2," *J. Fluid Mech.* **297**, 307–325 (1995).
- ¹⁷D. Homentcovschi and R. N. Miles, "A re-expansion method for determining the acoustical impedance and the scattering matrix for the waveguide discontinuity problem," *J. Acoust. Soc. Am.* **128**, 628–638 (2010).
- ¹⁸C. M. Linton and I. Thompson, "Resonant effects in scattering by periodic arrays," *Wave Motion* **44**, 167–175 (2007).
- ¹⁹C. M. Linton and P. McIver, *Handbook of Mathematical Techniques for Wave Structure Interactions* (Chapman and Hall, Boca Raton, FL, 2001), 320 pp.
- ²⁰J.-P. Groby, W. Lauriks, and, V. T. E., "Total absorption peak by use of a rigid frame porous layer backed by a rigid multi-irregularities grating," *J. Acoust. Soc. Am.* **127**, 2865–2874 (2010).
- ²¹B. Nennig, E. Perrey-Debain, and M. Ben Tahar, "A mode matching method for modelling dissipative silencers lined with poroelastic materials and containing mean flow," *J. Acoust. Soc. Am.* **128**, 3308–3320 (2010).
- ²²L. C. Botten, M. S. Craig, R. C. McPhedran, J. L. Adams, and R. J. Andrewartha, "The finitely conducting lamellar diffraction grating," *Opt. Acta* **28**, 1087–1102 (1981).
- ²³J. B. Lawrie and R. Kirby, "Mode-matching without root-finding: Application to a dissipative silencer," *J. Acoust. Soc. Am.* **119**, 2050–2061 (2006).
- ²⁴G. Gabard and R. J. Astley, "A computational mode-matching approach for sound propagation in three-dimensional ducts with flow," *J. Sound Vib.* **315**, 1103–1124 (2008).
- ²⁵S. Elhay and J. Kautsky, "Algorithm 655: IQPACK: FORTRAN subroutines for the weights of interpolatory quadratures," *ACM Trans. Math. Softw.* **13**, 399–415 (1987).
- ²⁶A. Cummings and I.-J. Chang, "Sound attenuation of a finite length dissipative flow duct silencer with internal mean flow in the absorbent," *J. Sound Vib.* **127**, 1–17 (1987).
- ²⁷B. Nennig, E. Perrey-Debain, and J.-D. Chazot, "The method of fundamental solutions for acoustic wave scattering by a single and a periodic array of poroelastic scatterers," *Eng. Anal. Bound. Elem.* **35**, 1019–1028 (2010).
- ²⁸O. Dazel and V. Tournat, "Nonlinear Biot waves in porous media with application to unconsolidated granular media," *J. Acoust. Soc. Am.* **127**, 692–702 (2009).
- ²⁹J.-F. Allard, M. Henry, and J. Tiziantel, "Sound propagation in air-saturated random packings of beads," *J. Acoust. Soc. Am.* **104**, 2004–2007 (1998).
- ³⁰B. Castagnède, M. Saeid, A. Moussatov, V. Gusev, and V. Tournat, "Reflexion and transmission at normal incidence onto air-saturated porous materials and direct measurements based on parametric demodulated ultrasonic waves," *Ultrasonics* **44**, 221–229 (2006).